Research Article | Vol. 32, No. 8 / 8 Apr 2024 / Optics Express 13628
Optics EXPRESS

Volume detection based on porous silicon waveguide for CO_2 mid-infrared spectroscopy

Sofiane Meziani,[1] Abdallah Jaafar,[1] Abdelali Hammouti,[1] Loïc Bodiou,[1] Nathalie Lorrain,[1] Parastesh Pirasteh,[1] Rémi Courson,[2] Jonathan Lemaitre,[1] Virginie Nazabal,[3] Mohammed Guendouz,[1] and Joël Charrier[1,*]

[1]Univ Rennes, CNRS, Institut Foton-UMR 6082, 22305 Lannion, France
[2]Ifremer, RDT Research and Technological Development, F-29280 Plouzané, France
[3]CNRS UMR 6226 ISCR, Université de Rennes, 22302 Rennes, France
[*]joel.charrier@univ-rennes.fr

Abstract: A mid-infrared (mid-IR) porous silicon (PSi) waveguide gas sensor was fabricated. PSi guiding and confinement layers were prepared by electrochemical anodization. Ridge waveguides were patterned using standard i-line photolithography and reactive ion etching. Due to the open pores, light and gas molecules interact in the inside volume, unlike bulk material in which the interaction takes place with the evanescent part of the light. Propagation losses are measured for a wavelength range spanning from $\lambda = 3.9$ to 4.55 µm with a value of 11.4 dB/cm at $\lambda = 4.28$ µm. The influence of native oxidation and ageing on the propagation losses was investigated. Limit of detection (LoD) of 1000 ppm is obtained with the waveguide sensor at the carbon dioxide (CO_2) absorption peak at $\lambda = 4.28$ µm.

1. Introduction

In recent years, there has been increasing scientific interest in the development of mid-infrared photonic circuits for optical sensing applications [1]. This is largely due to significant progress in the development of optical sources, such as QCL and supercontinuum sources [2] [3]. The mid-IR wavelength range is well-suited for optical sensing due to the absorption bands of several toxic and polluting molecules [4], making it well-placed to respond to diverse applications, including in-situ and harsh environments. The high level of performance needed for mid-IR sensors has created a demand for innovative materials and guiding structures. Integrated optical circuits offer several advantages, such as lower manufacturing costs and compact packaging, but require mid-IR transparent materials [5]. A well-recognized approach for integrated photonic sensing is the evanescent wave absorption spectroscopy. It is based on the fraction of the field extending outside the waveguide core interacting with the targeted analyte [6].

It has been shown that the most appropriate parameter for calculating the fraction of the electric field interacting with the targeted analyte is using the external confinement factor [7] [8] [9]. It expresses the sensitivity of the waveguide to refractive index variation in the active sensing region:

$$\Gamma = \frac{\partial n_{eff}}{\partial n_{superstrate}} \tag{1}$$

where n_{eff} *is* the effective refractive index and $n_{superstrate}$ the refractive index of the active sensing area. After developing (Eq. 1), the following formula is obtained:

$$\Gamma = \frac{n_g}{n_{superstrat}} \frac{\iint_{superstrate} \varepsilon \left|\vec{E}\right|^2 \mathrm{d}x\mathrm{d}y}{\iint_{\infty} \varepsilon \left|\vec{E}\right|^2 \mathrm{d}x\mathrm{d}y} \tag{2}$$

#516923 https://doi.org/10.1364/OE.516923
Journal © 2024 Received 3 Jan 2024; revised 28 Feb 2024; accepted 29 Feb 2024; published 28 Mar 2024

Optics EXPRESS

with n_g group index, ε the permittivity and $\vec{E}$ the electric field.

Some studies have investigated ways to improve the overlap factor in order to enhance the sensitivity of waveguide sensors. Incorporation of an under-cladding thin metal film for a strip silicon waveguide, elevates the guided mode toward the upper boundary and reduces the light confinement in the substrate region [10]. Improvement of the evanescent field ratio (*EFR)* by 10% was also performed for CO gas sensing application at $\lambda = 4.67$ µm. Enhancement of the *EFR* was also demonstrated with a dual hybrid plasmonic silicon waveguide. 20 µm length middle section of the waveguide was tapered on the entrees and 50 nm thickness gold layer was placed on both sides with a sub-wavelength gap. The achieved *EFR* was 74% for CH_4 sensing at $\lambda = 3.392$ µm [11]. Another study showed an external confinement factor $\Gamma = 44\%$ for CO_2 sensing at $\lambda = 4.24$ µm by suspending the silicon waveguide [12]. The evanescent field part below the waveguide is reached by analyte molecules unlike with standard ridge waveguide in which the active part is only on the top.

Volume sensing is another approach for integrated photonic absorption spectroscopy. The interaction with the molecules takes place deeper inside the waveguide, unlike evanescent field sensing which only occurs at the surface of the waveguide. Consequently, volume detection leads to a significantly higher light-matter interaction compared to evanescent wave interaction. However, this heightened interaction also results in increased propagation losses due to volume scattering [13]. This kind of interaction can be achieved by slot waveguide. A slot Ge-on-Si waveguide leads to the enhancement of Γ to reach 17.1% instead of 6.39% obtained with a standard ridge Ge-on-Si waveguide [14]. Volume interaction can also be accomplished with subwavelength waveguide. 5 ppm ammonia was experimentally detected by a 3 mm subwavelength grating cladding waveguide using InGaAs-InP material platform [15]. Theoretical power confinement factors of 40% and 50% are reported using slot waveguide and subwavelength grating slot sensors, respectively, with a silicon-on-sapphire platform for CO_2 sensing at $\lambda = 4.23$ µm [16].

Exploring porous materials, like nanoporous TiO_2 [17], porous Germanium [18] or porous silicon (PSi) [19], has been undertaken as a means to improve the sensibility of many different types of sensors. The use of optical integrated circuits made from a porous material improves the interaction with the optical guided mode and allows a volume detection with the analyte infiltration inside the porous layers [20]. PSi has great potential for mid-IR integrated circuits design. In addition to its CMOS-compatibility [21] and a transparency up to 8 µm, it enables refractive index and thickness tuning [22]. PSi feature pore diameters estimated in the range of [10 - 30 nm] [23] offering high specific surface up to 800 m^2cm^{-3} [24]. Moreover, PSi is also biocompatible material and the functionalization of its internal surface by passivating the layers with grafting specific biomolecules enables selectivity during the sensing application [25].

In this paper, the enhancement of the waveguide sensitivity using a ridge PSi waveguide is studied. A mid-IR optical bench setup is used to demonstrate CO_2 sensing application of the PSi waveguide. The optical transmission of the fabricated ridge waveguide is also carried out within the 3.9 to 4.55 µm wavelength range. We have previously explored the implementation of optical multilayer Bragg reflectors and microcavity from PSi layers for the mid-infrared [22]. This work, however, focuses on the use of porous layers for the development of integrated optical waveguides for sensing applications.

2. Materials and methods

To produce porous silicon (PSi) layers, a single-crystal silicon substrate is anodized electrochemically by immersing it in an electrolyte that contains a hydrofluoric acid-based solution (HF). The anode is the silicon substrate, and an electric current is applied between the silicon substrate and a platinum cathode electrode, which is chosen for its resistance to HF [26]. The electrical contact for the anode is located on the back side of the silicon substrate.

Optics EXPRESS

In this work, guiding and cladding PSi layers were obtained using a heavily doped P (100) silicon substrate with a 5 mΩ.cm resistivity and using applied current densities of 50 and 100 mA/cm^2, during 65 and 102 seconds respectively. The electrolyte was formed by combining hydrofluoric acid (50%) with ethanol and deionized water in the ratio of 2-2-1.

Refractive index is tuned by changing the porosity that depends on applied current density. In this way, two layers were fabricated: a 2.2 µm guiding layer with a porosity of 60% and a 5 µm confinement layer with a porosity of 73% with corresponding refractive indices equal to 1.71 and 1.48 at 4.28 µm respectively. The refractive index for each of the fabricated PSi layer was deduced from FTIR reflectance spectra, by fitting experimental spectral fringes and applying the Bruggeman effective medium approximation theory [27] as shown in Fig. 1.

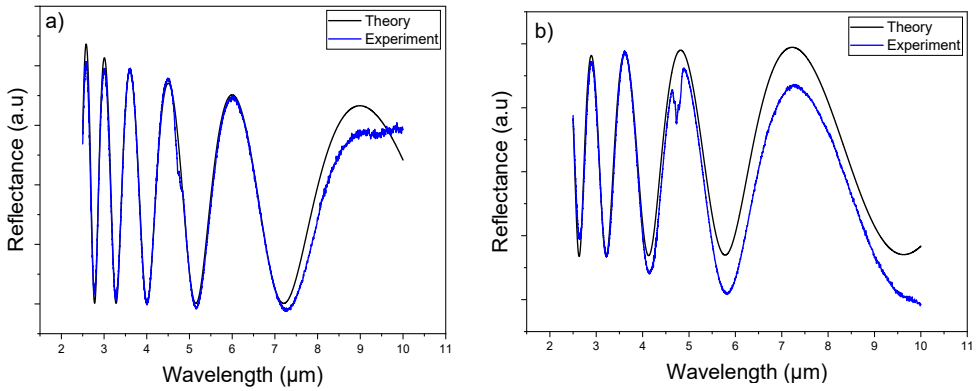

Fig. 1. FTIR reflectance spectra for a) the guiding layer b) the confinement layer.

Ridge waveguides were fabricated (Fig. 2(a)) using a standard photolithographic process. A positive photosensitive resin layer (S1813) was deposited by spin coating on the top of the structure. Patterns were then produced under UV exposure through a chrome mask designed using matlab and Klayout softwares. The process continues with a low-pressure dry etching, combining reactive ion etching (RIE) and inductively coupled plasma (ICP) etching with CHF_3 gas. The remaining resin was removed using an O_2 plasma. The photolithography mask used consists of several sets of waveguides with different lengths (Fig. 2(b)). This configuration allows propagation loss measurements using a non-destructive cut-back method.

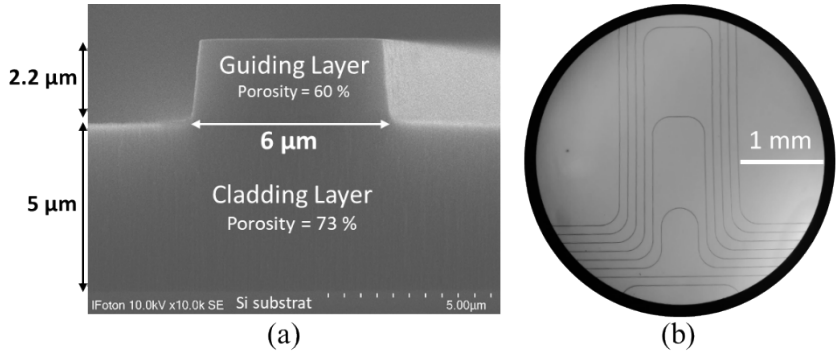

Fig. 2. View of the fabricated PSi ridge waveguides (a) SEM Image (b) Optical microscope top view.

Optics EXPRESS

Prior to the fabrication step, the ridge waveguide structures were designed using a commercial software (*FIMMWAVE, Photon Design*) to obtain single mode structure with a width equal to 6 µm and a height equal to 2.2 µm. Mode propagation cartography is simulated as illustrated in Fig. 3(a). Considering the porosities, the external confinement factor (Γ) is calculated for each layer of the PSi waveguide: superstrate which is air here, guiding and cladding layer, as showed on Fig. 3(b). The expression in Eq. (2) becomes after developing:

$$\Gamma = n_g\left(\frac{S_{air} + \varepsilon_{guide} S_{guide} Porosity_{guide} + \varepsilon_{clad} S_{clad} Porosity_{clad}}{S_{air} + \varepsilon_{guide} S_{guide} + \varepsilon_{clad} S_{clad}}\right) \quad (3)$$

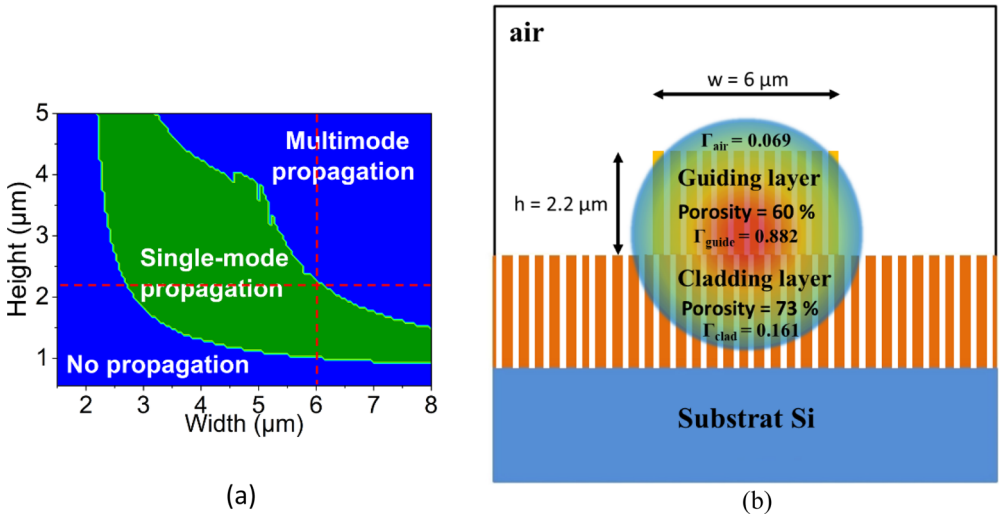

Fig. 3. (a) Cartography the propagation mode at λ = 4.28 µm as a function of the dimension of the PSi waveguide with a projection of the fabricated waveguide dimension. (b) Scheme of the fabricated PSi waveguide and the guided mode TE00

With n_g representing the group index, ε_{guide} and ε_{clad} denoting the permittivity in the guide and cladding layer, respectively, S_{air}, S_{guide} and S_{Clad} are the integrals of the square of the field in the air, guiding, and cladding regions, respectively. The areas occupied by the future analyte are described by $Porosity_{guide}$ in the guiding layer and $Porosity_{clad}$ in the cladding layer. The total external confinement factor then is estimated being $\Gamma_{TE} = 111\%$ at λ = 4.28 µm for the fundamental TE mode and $\Gamma_{TM} = 115\%$ for TM mode.

The observed interaction within this porous structure can be analogized to that occurring in free space sensing, characterized by elevated optical parameters as defined by Bruggeman's model, rather than those typical of air. This leads to a higher group index, consequently yielding an external confinement factor surpassing unity.

3. Result and discussion

3.1. Optical bench and characterization of the guiding structures

Optical characterizations were performed by the mid-IR bench presented in Fig. 4. To make the mid-IR waveguide coupling easier, a NIR source is used at first. Optical signal at λ = 1.55 µm is coupled into the PSi waveguide by using microstructured single-mode chalcogenide glass fiber, thus defining an optical axis. Then, a tunable QCL emitting from λ = 3.9 to 4.6 µm (*MIRCAT, Daylight Solutions*) was aligned on the same optical axis to achieve the mid-IR coupling. The output signal from the waveguide was collimated to a detector (*DSS-PSE020TC, Horiba*), using

Optics EXPRESS

a mid-IR objective lens. To improve signal to noise ratio, lock-in technique was used. The QCL emission is polarized perpendicular to the base of the laser but as the coupling is achieved with a fiber, the polarization at the output of the fiber is modified. To properly perform the optical characterizations, the position of the chalcogenide glass fiber should be fixed the whole of the measurement to maintain the same coupling mode [28]. Since the polarization of the mode is affected by the fiber, the coupled mode into the PSi ridge waveguide can be a random composition of the two fundamental modes TM and TE. Consequently, the value of Γ should take a value between Γ_{TE} and Γ_{TM}.

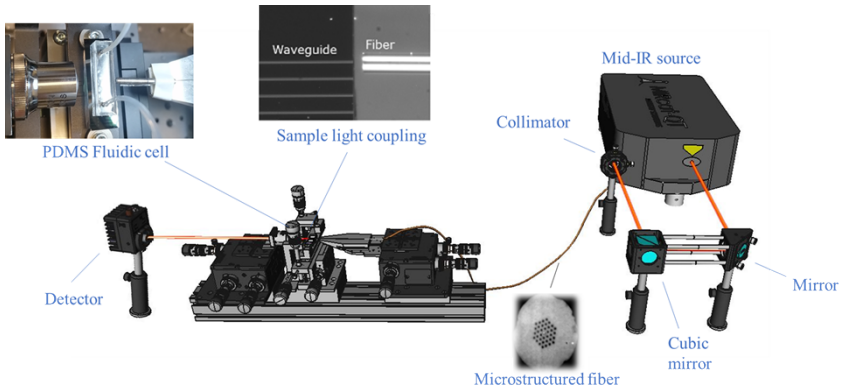

Fig. 4. Schematic diagram of the optical bench platform sensor.

Using mid-IR optical characterization bench, the transmission was measured for all waveguide's lengths (6.3, 7.3, 9.3, 11.3, 13.3, 15.3, 17.3 mm) for wavelengths ranging from 3.9 µm to 4.55 µm. Detector response demonstrates an exponential decline with increasing length, as depicted in Fig. 5(a), owing to propagation losses. The spectra exhibit identical spectral signatures for all seven lengths of the waveguides, with no observed overlap. This supports the notion that the propagation is single mode. The behavior of the signal can be determined by Beer-Lambert law:

$$P(\lambda) = P_0(\lambda)e^{-(\epsilon(\lambda)\Gamma(\lambda)CL_{analyte})}e^{-(\alpha(\lambda)L_{waveguide})} \quad (4)$$

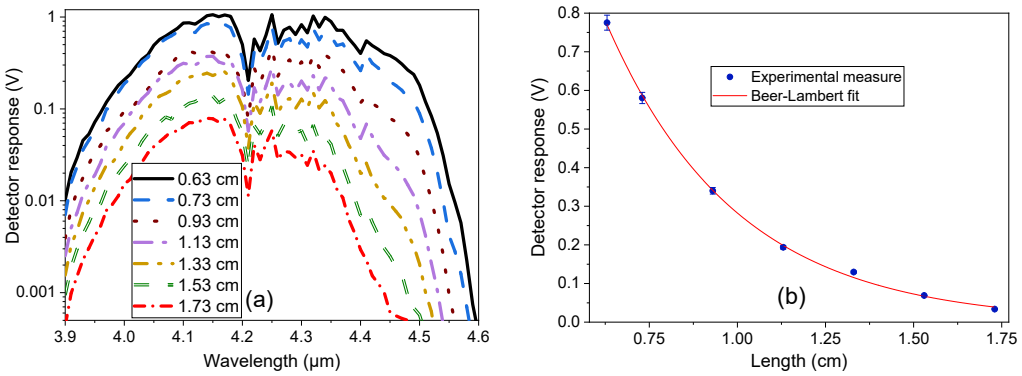

Fig. 5. (a) Evolution of the signal amplitude as a function of the wavelength for all waveguide's lengths. (b) Signal amplitude as a function of the waveguide length for a fixed wavelength at $\lambda = 4.28$ µm with Beer-Lambert fit.

With P_0 the initial amplitude, ε the absorption coefficient, Γ the external confinement factor, C the analyte concentration, $L_{analyte}$ the interaction length between the analyte and the optical mode,

Optics EXPRESS

α the propagation loss and $L_{waveguide}$ the length of the waveguide. Since no specific analyte is being targeted in the measurement of the propagation losses, it is assumed that the concentrations of molecules present in the ambient air do not significantly variate during the acquisitions. The absorption term in Eq. (4) can be then included in $P_0(\lambda)$.

Figure 5(b) shows the signal amplitude for each waveguide length at a fixed wavelength $\lambda = 4.28$ µm with the applied fit. The propagation loss $\alpha(\lambda)$ is then extracted from the fit. The same operation is repeated for all the scanned wavelengths from 3.9 to 4.55 µm.

Figure 6(a) illustrates the evolution of the propagation losses for the PSi sample at 3 different times after the fabrication of the sample: as prepared, after 8 days and after 10 days. The first two measurements aim to study the ageing of the sample. There is a broad similarity between these two measurements except a slight increase on the losses caused probably by the formation of thin film of silica at the surface of the pores due to ambient air infiltration. The last measurement 10 days after the fabrication, is performed after soaking the sample in a 5% hydrofluoric acid solution for 1 minute. The soaking removes the native silica layer and desorbs molecules from the pores. The propagation losses decrease by around 5 dB/cm from $\lambda = 3.90$ µm to 4.19 µm and by 10 dB/cm after $\lambda = 4.20$ µm. The sample transparency range also increases by extending the limit transparency wavelength range from 4.36 to 4.55 µm. So, a value of 11.4 dB/cm is measured at $\lambda = 4.28$ µm.

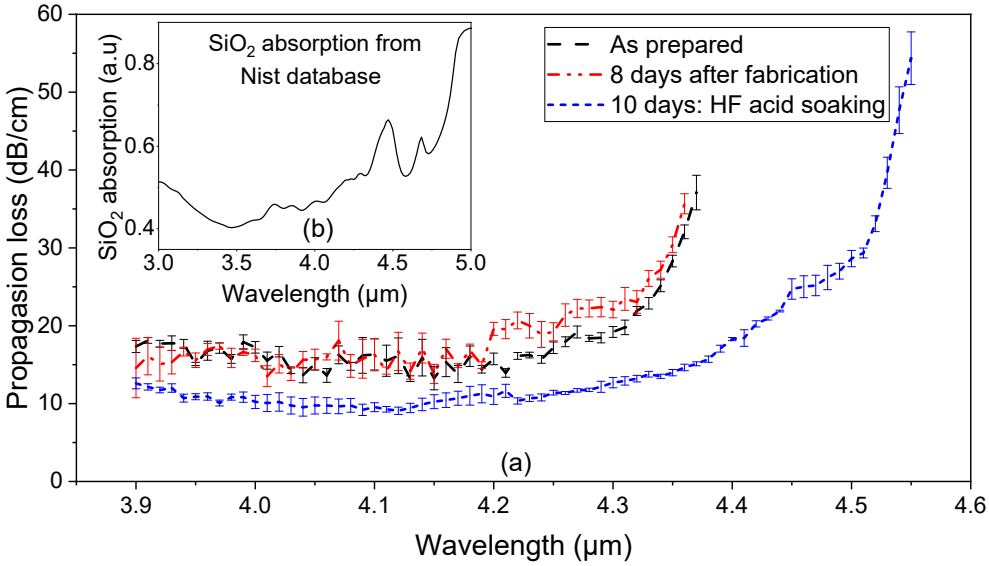

Fig. 6. (a) Propagation loss as a function of the wavelength for porous silicon ridge waveguides. The measure was achieved at 3 different times: as prepared and after 8 and 10 days of the fabrication of the sample. (b) Absorption spectrum at room temperature of fused silica reproduced from NIST database

The measured losses for PSi platform are high compared to other platforms on the same wavelength range [29] [30]. These high loss values result mainly from free carrier absorption in the heavily doped bulk silicon substrate [31] and scattering [32] but also from adsorption of different molecules present in ambient air inside the pores. Silicon oxide is also formed on the surface of the sample by interaction with the ambient air. The absorption of silicon oxide in the working wavelength range increases the propagation losses as shown in Fig. 6(b). To measure the propagation losses, a fit related to Eq. (4) was applied to the experimental measurements. Since no specific analyte is being targeted in the propagation loss measurement, it is assumed that the

Optics EXPRESS

concentrations of other molecules present in the ambient air do not significantly vary during the measurements. The absorption term in Eq. (4) can be then included in $P_0(\lambda)$.

3.2. Sensing demonstration

To evaluate the sensing capacity of the PSi platform, transduction tests are carried out for carbon dioxide. Different concentrations of CO_2 diluted with N_2 are prepared. Flexible pipes provide the mixture from two gas cylinders of 100% concentration of N_2 and CO_2 by two mass flows of 100 sccm and 50 sccm respectively. A flow rate controller is used to regulate the CO_2 - N_2 gas mixture during the sensing tests. To make the gas in contact with the ridge waveguide, a PDMS cell (microchannel of 140 µm thick, 5 mm wide and 28 mm long) is bonded on the sample as shown in Fig. 7.

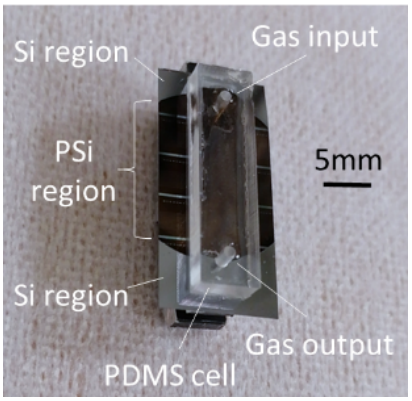

Fig. 7. PDMS fluidic cell used for sensing tests.

The theoretically optimal interaction length is estimated to be equal to 4 mm [33]. However, in this study, a PDMS cell enabling an interaction length of 8.3 mm is used. The stability and regeneration of the sensor application is demonstrated by recording the time dependent intensity at a fixed wavelength $\lambda = 4.26$ µm and increasing gradually CO_2 concentration from 0.0% to 9.09% and then decreasing it gradually until 0.0%. The measurements during both decreasing and increasing transmissions demonstrated a strong correlation between optical signals and CO_2 concentration levels (Fig. 8).

The fact that identical signal amplitude levels are observed for the same concentration during both increasing and decreasing concentration serves as evidence of the sensing reproducibility of the porous layers. The stability of the signal is obtained a few tens of seconds after changing the CO_2 concentration. The evaluation of the time response time of the sensor will be more accurate if the fluidic piping system is considered. The same measurement on the maxima absorption peaks at 4.23 and 4.28 µm yielded much sharper change in level with much noisier curves.

To highlight the detection of CO_2 through spectral analysis, the transmission spectra of the PSi platform sensor are measured for different CO_2 concentrations, with 8.3 mm as length of interaction between the PSi waveguide and the gas mixture. Detector response demonstrates an exponential decline with increasing concentration due to CO_2 absorption. The maximum peak of absorption recorded corresponds to the two tabulated absorption lines of CO_2 at 4.23 µm and 4.28 µm from HITRAN database (Fig. 9(a)) [34]. The normalized transmission spectra are shown in Fig. 9(b) for λ varying from 4.14 to 4.33 µm for different defined CO_2 concentration.

There is decay between the two maxima peaks level because the signal baseline exhibits an inclination. This is a result of a slight displacement of the stages that supported the coupling

Optics EXPRESS

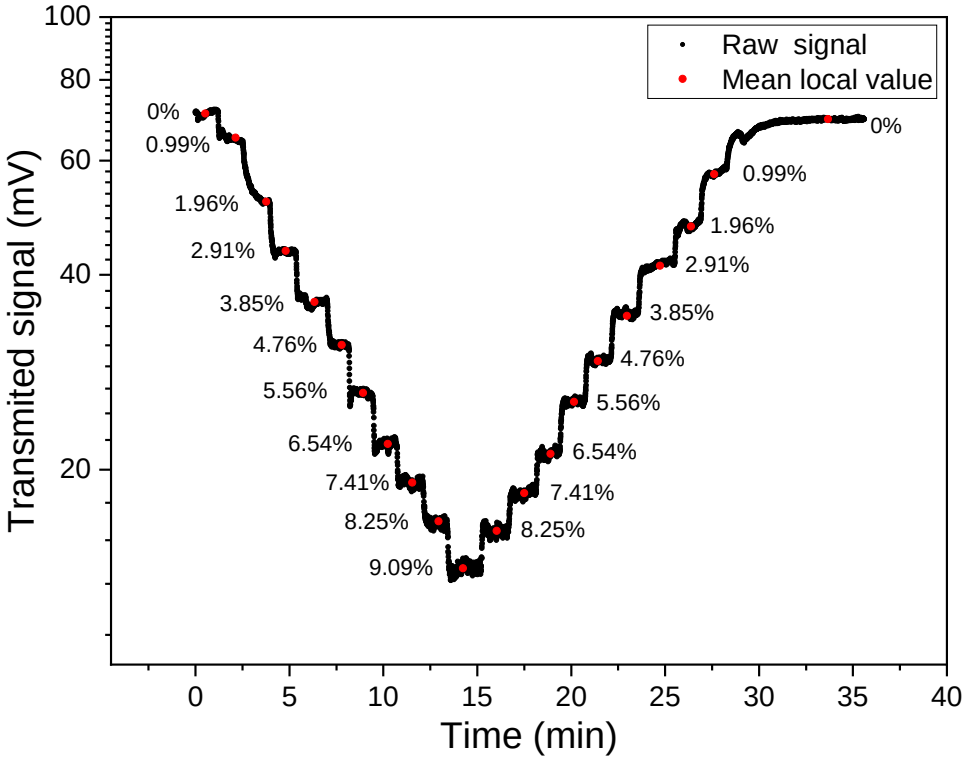

Fig. 8. Intensity evolution of the transmitted signal at fixed laser emission ($\lambda = 4.26$ µm) with increasing and then decreasing CO_2 concentration.

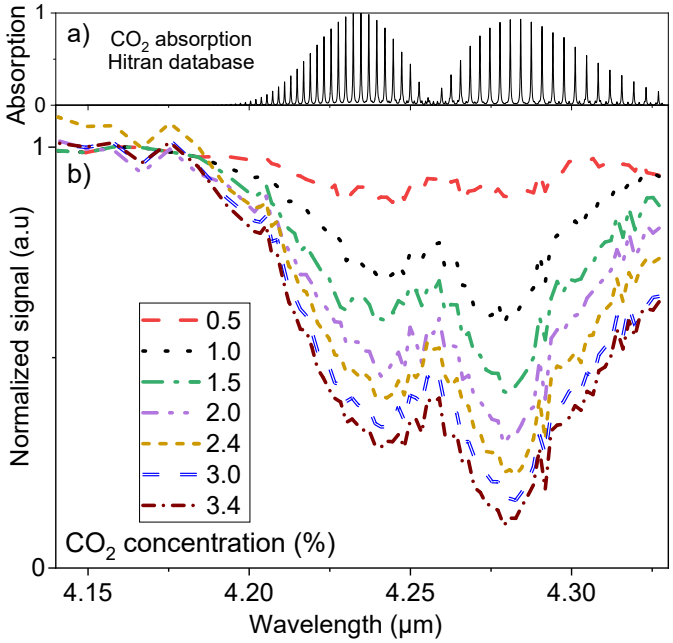

Fig. 9. a) Normalized CO_2 Absorption from 4.14 to 4.33 µm from HITRAN database [34]. b) Normalized PSi waveguide transmission spectra for different CO_2 concentrations.

Optics EXPRESS

fiber during a few tens of minutes wavelength scan. It will be interesting to use motorized stages capable of real-time self-alignment for the input fiber to make the measurement more accurate.

In waveguide-based optical sensors, the Beer-Lambert formula (Eq. (4)) assumes a fixed waveguide length, allowing the propagation loss term to be treated as a constant that can be included in the amplitude of the signal $P_0(\lambda)$. A fit considering the CO_2 absorption is applied on experimental signal amplitude measured at different CO_2 concentration for a fixed wavelength at $\lambda = 4.28$ µm using an interaction length of 8.3 mm. Figure 10 shows a good agreement between the experimental measurement and the Beer-Lambert fit. According to the experiment parameters and the fit, the product ε x Γ can be extracted. We find a value between 52.2 and 54.1 cm^{-1} for ε at $\lambda = 4.28$ µm, using the simulated values of Γ. The experimental estimation of both parameters ε and Γ with a good precision becomes challenging due to the line width of the laser and the presence of a section of the beam that propagates in free space before and after interacting with the sample.

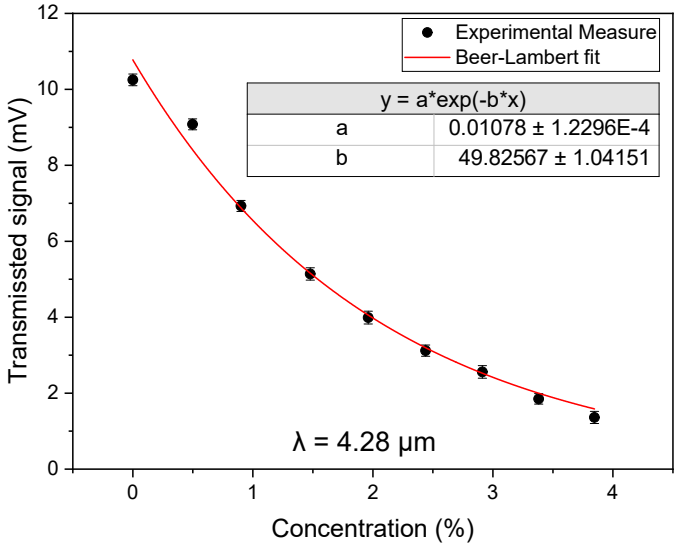

Fig. 10. Signal amplitude as a function of CO_2 concentration for a wavelength fixed at $\lambda = 4.28$ µm and waveguide length fixed to L = 8.3 mm.

The lower concentration of CO_2 that was detected with the PSi platform at $\lambda = 4.28$ µm was 4980 ppm as shown in Fig. 11. The Limit of Detection (LoD) represents the smallest concentration of the analyte that the sensor can detect [35]. And this LoD can be determined by the following equation:

$$\mathrm{LoD} = 3.3\frac{\sigma}{\mathrm{S}} \tag{5}$$

with σ is the system noise variance (equal to 1.55 10^{-4} Volt) and S the sensitivity (equal to 0.51 Volt. $(v/V)^{-1}$ calculated from Fig. 10 where (v/V) is the concentration ratio). A LoD of 1000 ppm is estimated from these experimental data.

Table 1 illustrates the comparison between the proposed sensor and other gas sensors. LoD in [36] is higher despite the lower propagation losses, this can be explained by their weak overlap factor. With an Γ estimated at 44% and lower propagation losses of 3 dB/cm, a LoD of 1000 ppm of CO_2 is measured in [12] which is similar to this work despite our higher propagation losses. The low LoD value obtained in [37] with lower propagation losses and lower overlap factor, can be explained by the stability of the laser and detector used during the measurement. The acquisition time would also have been optimized to reach such LoD without WMS (Wavelength Modulation

Optics EXPRESS

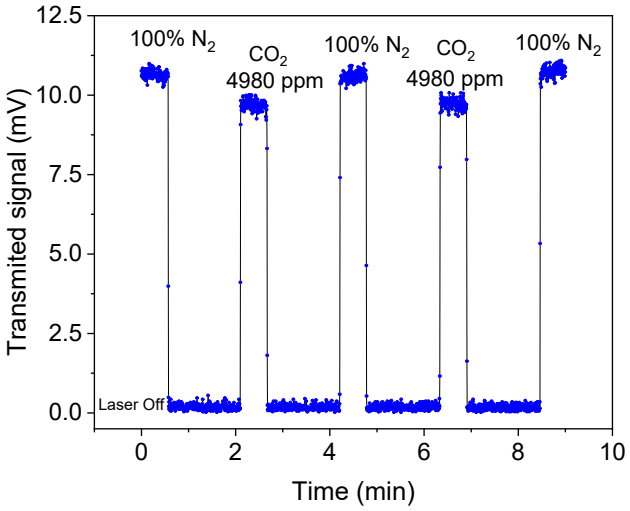

Fig. 11. Signal amplitude during several minutes with two levels of CO_2 concentration: 0 and 4980 ppm at fixed wavelength of $\lambda = 4.28$ µm and waveguide length fixed to L = 8.3 mm. The laser is turned off after each concentration change

Spectroscopy). According to Ref. [38], concentrations of 2.6 ppb (parts per billion) can be achieved as theorical LoD, but it requires laser stability and detection noise level significantly higher than those used in current experiments.

Table 1. Comparison of the CO_2 sensing with the state-of-the-art

λ (µm)	Analyte	Study	Waveguide	length (cm)	Loss (dB/cm)	Γ (%)	LoD (ppm)	FOM	Ref
4.67	CO	Theorical	SiGe slot	-	0.5	88.3	0.0026	7.66	[38]
4.319	CO_2	experimental	ChGs ridge	1	5.1	4.6	25000	0.04	[36]
4.23	CO_2	experimental	Si ridge	2	3.98	16	500	0.17	[37]
4.24	CO_2	experimental	Si suspended	0.32	3	44	1000	0.64	[12]
4.28	CO_2	experimental	PSi ridge	0.83	11.4	115	1000	0.44	This work

The performance of experimental optical integrated sensors can be evaluated by calculating the figure of merit (*FOM*) based on the propagation losses and the overlap factor. It is defined as following:

$$FOM = \frac{\Gamma}{\alpha} \tag{6}$$

It shows that minimizing the propagation losses and maximizing the external confinement factor make FOM higher. In contrast to comparing based on the LoD as a criterion, comparing sensors FOM does not consider the parameters of the laser source and the detector, particularly their stability and resolution. This criterion restricts the comparison only to the transducer part. The FOM of the PSi fabricated sensor is higher than FOM in [37] despite their 500 ppm LoD. It is also very close to the FOM of Ref. [12] which is the highest among the different compared sensors.

Optics EXPRESS

4. Conclusion

The optical properties of porous silicon are demonstrated through the fabrication of a ridge PSi waveguide as a volume transducer. The infiltration of analytes inside the core of the integrated circuit significantly enhances the external confinement factor, surpassing unity and enabling a 115% overlap factor for the TM fundamental mode. Initially, propagation losses of the PSi waveguide were measured in the range of 3.9 to 4.55 µm. Following that, carbon dioxide sensing was investigated at absorption peak at $\lambda = 4.28$ µm, achieving CO_2 detection down to a concentration of 4980 ppm with the PSi platform. Despite high propagation losses in the PSi structure, the estimated LoD of 1000 ppm is in the same range as the state of the art. The optimization of technological processing is currently being carried out on PSi integrated circuits to reduce the propagation losses and improve their sensing performance. Better sensing results are also expected by reducing the interaction length to the estimated optimum value equal to 4 mm. Functionalization of PSi layers by grafting molecules is under study to make selectivity during the sensing. Finally, WMS can be also employed to further lower the LoD.

Funding. Lannionnais Trégor Communauté; Conseil Régional de Bretagne (CPER Sophie); Agence Nationale de la Recherche (ANR ANR-21-CE04-001, ANR-17-CE09-0028-01).

Acknowledgments. The PSi waveguide fabrication was performed in the Centre Commun Lannion d'Optique (CCLO)–technological platform which is supported by the French RENATECH + network.

Disclosures. The authors declare no conflicts of interest.

Data availability. Data underlying the results presented in this paper are not publicly available at this time but may be obtained from the authors upon reasonable request.

References

1. M. A. Kanjwal and A. A. Ghaferi, "Advanced Waveguide Based LOC Biosensors: A Minireview," Sensors **22**(14), 5443 (2022).
2. A. Spott, Jon Peters, Michael L. Davenport, *et al.*, "Quantum cascade laser on silicon," Optica **3**(5), 545–551 (2016).
3. F. Cheng, Jinchuan Zhang, Yanjiao Guan, *et al.*, "Ultralow power consumption of a quantum cascade laser operating in continuous-wave mode at room temperature," Opt. Express **28**(24), 36497–36504 (2020).
4. J. Wu, Gongcheng Yue, Weicheng Chen, *et al.*, "On-Chip Optical Gas Sensors Based on Group-IV Materials," ACS Photonics **7**(11), 2923 (2020).
5. A. Yadav and A. M. Agarwal, "Integrated photonic materials for the mid-infrared," Int. J. Appl. Glass Sci. **11**(3), 491–510 (2020).
6. M. Sieger and B. Mizaikoff, "Toward On-Chip Mid-Infrared Sensors," Anal. Chem. **88**(11), 5562–5573 (2016).
7. G. J. Veldhuis, O. Parriaux, H. J. W. M. Hoekstra, *et al.*, "Sensitivity enhancement in evanescent optical waveguide sensors," J. Lightwave Technol. **18**(5), 677–682 (2000).
8. C. Consani, F. Dubois, and G. Auböck, "Figures of merit for mid-IR evanescent-wave absorption sensors and their simulation by FEM methods," Opt. Express **29**(7), 9723–9736 (2021).
9. J. T. Robinson, K. Preston, O. Painter, *et al.*, "First-principle derivation of gain in high-index-contrast waveguides," Opt. Express **16**(21), 16659–16669 (2008).
10. M. A. Butt, S. N. Khonina, and N. L. Kazanskiy, "Enhancement of evanescent field ratio in a silicon strip waveguide by incorporating a thin metal film," Laser Phys. **29**(7), 076202 (2019).
11. S. N. Khonina, N. L. Kazanskiy, and M. A. Butt, "Evanescent Field Ratio Enhancement of a Modified Ridge Waveguide Structure for Methane Gas Sensing Application," IEEE Sensors J. **20**(15), 8469–8476 (2020).
12. F. Ottonello-Briano, C. Errando-Herranz, H. Rödjegård, *et al.*, "Carbon dioxide absorption spectroscopy with a mid-infrared silicon photonic waveguide," Opt. Lett. **45**(1), 109–112 (2020).
13. P. Azuelos, Pauline Girault, Nathalie Lorrain, *et al.*, "Optimization of porous silicon waveguide design for micro-ring resonator sensing applications," J. Opt. **20**(8), 085301 (2018).
14. J. Lim, J. Shim, D.-M. Geum, *et al.*, "Experimental Demonstration of Germanium-on-Silicon Slot Waveguides at Mid-Infrared Wavelength," IEEE Photonics J. **14**(3), 1–9 (2022).
15. K. M. Yoo, J. Midkiff, A. Rostamian, *et al.*, "InGaAs Membrane Waveguide: A Promising Platform for Monolithic Integrated Mid-Infrared Optical Gas Sensor," ACS Sens. **5**(3), 861–869 (2020).
16. Y. Song, B. Li, H. Zhang, *et al.*, "Silicon Waveguide Sensors for Carbon Dioxide Gas Sensing in the Mid-Infrared Region," Photonics **10**(2), 120 (2023).
17. Z.-M. Qi, I. Honma, and H. Zhou, "Nanoporous leaky waveguide based chemical and biological sensors with broadband spectroscopy," Appl. Phys. Lett. **90**(1), 011102 (2007).

Optics EXPRESS

18. R. Zegadi, Sofiane Meziani, Sofiane Meziani, *et al.*, "Theoretical Demonstration of the Interest of Using Porous Germanium to Fabricate Multilayer Vertical Optical Structures for the Detection of SF6 Gas in the Mid-Infrared," Sensors **22**(3), 844 (2022).
19. G. Rong, Ali Najmaie, John E Sipe, *et al.*, "Nanoscale porous silicon waveguides for biosensing applications," in *LEOS 2008 - 21st Annual Meeting of the IEEE Lasers and Electro-Optics Society* 2008, p. 340–341.
20. G. D. Allen, W. F. Delaney, and J. D. Ryckman, "Porous Silicon Photonics at Unity Confinement Factors for Biosensing Applications," in *2018 Conference on Lasers and Electro-Optics (CLEO)*, 2018, p. 1–2.
21. G. Barillaro, P. Bruschi, F. Pieri, *et al.*, "CMOS-compatible fabrication of porous silicon gas sensors and their readout electronics on the same chip," Physica Status Solidi (a) **204**(5), 1423–1428 (2007).
22. M. Duris, Yannick Coffinier, V. Thomy, *et al.*, "Vertical multilayer structures based on porous silicon layers for mid-infrared applications," Opt. Mater. Express **10**(8), 1921–1930 (2020).
23. N. Lorrain, P. Pirasteh, P. Girault, *et al.*, "Submicron gap reduction of micro-resonator based on porous silica ridge waveguides manufactured by standard photolithographic process," Opt. Mater. **88**, 210–217 (2019).
24. A. Loni, "Porous Silicon Formation by Anodization," in Handbook of Porous Silicon, L. Canham, Éd., Cham: Springer International Publishing, 2014, p. 11–22.
25. L. De Stefano, Paolo Arcari, Annalisa Lamberti, *et al.*, "DNA Optical Detection Based on Porous Silicon Technology: from Biosensors to Biochips," Sensors **7**(2), 214–221 (2007).
26. A. Shokrollahi and M. Zare, "Fabricating optical waveguide based on porous silicon structures," Optik **124**(9), 855–858 (2013).
27. J. E. Spanier and I. P. Herman, "Use of hybrid phenomenological and statistical effective-medium theories of dielectric functions to model the infrared reflectance of porous SiC films," Phys. Rev. B **61**(15), 10437–10450 (2000).
28. J. D. LeGrange, H. C. Ling, and D. M. Velez, "Effects of mechanical stress on the transmission properties of optical fiber packaged in a composite structure," Appl. Opt. **33**(18), 3890–3895 (1994).
29. R. Shankar, I. Bulu, and M. Lončar, "Integrated high-quality factor silicon-on-sapphire ring resonators for the mid-infrared," Appl. Phys. Lett. **102**(5), 051108 (2013).
30. M. Brun, Pierre Labeye, Gilles Grand, *et al.*, "Low loss SiGe graded index waveguides for mid-IR applications," Opt. Express **22**(1), 508 (2014).
31. D. K. Schroder, R. N. Thomas, and J. C. Swartz, "Free carrier absorption in silicon," IEEE Trans. Electron Devices **25**(2), 254–261 (1978).
32. P. Ferrand and R. Romestain, "Optical losses in porous silicon waveguides in the near-infrared: Effects of scattering," Appl. Phys. Lett. **77**(22), 3535–3537 (2000).
33. A. Gutierrez-Arroyo, Emeline Baudet, Loïc Bodiou, *et al.*, "Theoretical study of an evanescent optical integrated sensor for multipurpose detection of gases and liquids in the Mid-Infrared," Sens. Actuators, B **242**, 842–848 (2017).
34. I. E. Gordon, L.S. Rothman, C. Hill, *et al.*, "The HITRAN2016 molecular spectroscopic database," J. Quant. Spectrosc. Radiat. Transfer **203**, 3–69 (2017).
35. B. W. Pack, S. Stithit, and W. Chen, "Clinical Supplies Manufacture," in Developing Solid Oral Dosage Forms, Elsevier, (2017), 653–676.
36. M. Pi, Chuantao Zheng, Huan Zhaoa, *et al.*, "Mid-infrared ChG-on-MgF_2 waveguide gas sensor based on wavelength modulation spectroscopy," Opt. Lett. **46**(19), 4797 (2021).
37. C. Ranacher, Cristina Consani, Natalie Vollert, *et al.*, "Characterization of Evanescent Field Gas Sensor Structures Based on Silicon Photonics," IEEE Photonics J. **10**(5), 1–14 (2018).
38. H. Kumar, T. Bohra, A. Sharma, *et al.*, "Polarization diversity schemes for gas sensing applications: a comprehensive analysis and optimal design of high-performance $S\,i_{1-x}G\,e_x$ mid-infrared asymmetric rib cross-slot waveguides," J. Opt. Soc. Am. B **40**(12), 3246–3254 (2023).